Check for updates

Biphasic anion-exchange nanofibers enable bipolar junction engineering for enhanced electrocatalytic CO_2 conversion in acidic media†

Peng Liu,‡[a] Fenglei Lyu, ‡[ab] Xiya Yang,[a] Zhangyi Zheng,[a] Wei Hua,[a] Shiwei Mei,[a] Mutian Ma,[a] Haojun Wang,[a] Xiaolin Ge, [c] Liang Wu, [c] Tongwen Xu, [c] Zhao Deng [ab] and Yang Peng *[abd]

Driven by renewable energies, electrocatalytic CO_2 reduction (eCO_2R) in acidic media using membrane electrode assemblies (MEAs) has emerged as a highly promising approach for large-scale CO_2 utilization with economic viability. Nevertheless, the practical implementation faces significant challenges, including competing hydrogen evolution reaction, salt precipitation, and water flooding, which collectively undermine the long-term faradaic efficiency and operational durability. In this work, we develop an innovative asymmetric porous bipolar membrane (BPM) architecture by integrating electrospun anion-exchange nanofibers with a planar cation-exchange membrane, and configure it in the forward-bias mode (f-BPM) within MEAs to enable efficient acidic eCO_2R. The biphasic anion-exchange nanofibers, comprising polycationic piperidinium copolymer and hydrophobic polyvinylidene difluoride, are engineered to simultaneously optimize ion conductivity, membrane swelling, and mechanical integrity, thereby effectively regulating cation migration, electrochemical impedance, and water and gas transport properties. The optimized f-BPM configuration demonstrates exceptional performance, maintaining stable operation for 325 hours in acidic conditions, while achieving an average CO faradaic efficiency of 88% and a remarkable single-pass CO_2 conversion efficiency of 67% at a current density of 300 mA cm^{-2} with a CO_2 flow rate of 15 sccm. Furthermore, the scalability of this technology is successfully demonstrated through the fabrication of a larger 5×5 cm^2 f-BPM, showcasing a stable operation over 110 hours with an energy efficiency of 34.2%. This breakthrough represents a significant advancement in acidic MEA technology, marking a crucial step toward industrial-scale implementation of eCO_2R.

Broader context

Electrocatalytic CO_2 reduction (eCO_2R) into valuable chemicals using renewable electricity is a promising strategy to mitigate climate change and achieve carbon neutrality. Its operation in acidic electrolyte is highly desirable due to the alleviated carbon loss, but faces severe challenges, including competing hydrogen evolution reactions (HERs), salt precipitation, and water flooding, which collectively undermine the current efficiency and long-term stability. This work, by introducing an innovative asymmetric porous bipolar membrane (BPM) architecture through the integration of electrospun anion-exchange nanofibers (AENFs) with a planar cation-exchange membrane (CEM), addresses critical challenges in eCO_2R under acidic conditions, offering a novel approach to enhance the efficiency, stability, and scalability of membrane electrode assemblies (MEAs) for industrial CO_2 utilization. The optimized BPM configuration demonstrates exceptional performance, achieving stable operation for 325 hours in acidic conditions with an average CO faradaic efficiency of 88% and a remarkable single-pass CO_2 conversion efficiency of 67% at 300 mA cm^{-2} under 15 sccm CO_2 flow. Furthermore, a 25 cm^2 scale-up MEA is demonstrated, maintaining stable operation over 110 hours with an energy efficiency of 34.2%, outperforming previous benchmarks. This breakthrough has the potential to significantly reduce carbon emissions and combat climate change.

[a] Soochow Institute for Energy and Material Innovations, College of Energy, Soochow University, Suzhou, 215006, China. E-mail: ypeng@suda.edu.cn

[b] Jiangsu Key Laboratory for Advanced Negative Carbon Technologies, Soochow University, Suzhou, 215123, China

[c] State Key Laboratory of Precision and Intelligent Chemistry, School of Chemistry and Materials Science, University of Science and Technology of China, Hefei, Anhui, 230026, China

[d] State Key Laboratory of Coordination Chemistry, School of Chemistry and Chemical Engineering, Nanjing University, Nanjing 210093, China

‡ These authors contributed equally to this work.

Introduction

Electrocatalytic CO_2 reduction (eCO$_2$R) powered by renewable electricity represents one of the most promising technologies today to resourcefully recycle anthropogenic CO_2.[1–3] Concerning the kinetic energy penalty, two-electron reduction products such as carbon monoxide (CO) and formic acid (HCOOH) are more likely to realize a profitable production in the foreseeable future based on recent techno-economic assessments.[4–6] With regard to the electrolyzer design, zero-gap membrane electrode assemblies (MEAs) operated under alkaline/neutral conditions are state-of-the-art, owing to the improved CO_2 mass transport, reduced ohmic losses, and favored chemical environment (Scheme 1a).[3,7–9] However, the use of anion-exchange membranes (AEMs) in these systems introduces significant challenges. AEMs facilitate the transport of large (bi)carbonate ions formed by the reaction of CO_2 with hydroxyl anions, leading to CO_2 crossover and increased ion migration resistance.[10,11] Moreover, the alkali cations would inevitably migrate to the cathode through co-ion leakage, precipitated as (bi)carbonate salts to restrain CO_2 transport on the gas diffusion electrode (GDE). This would further exacerbate disastrous issues such as the hydrogen evolution reaction (HER) and water flooding.[12] Thus, before the AEM-based MEA can be practically deployed, issues of CO_2 crossover and salt precipitation must be addressed for extended efficiency and stability.

eCO$_2$R under acidic conditions using cation exchange membranes (CEMs) can effectively sidestep the above issues of CO_2 crossover (Scheme 1b).[3,13–16] The migration of anions from the cathode to the anode can be mostly blockaded by the fixed anionic groups in CEM via Donnan exclusion.[17] The formation of (bi)carbonate salts in the gas diffusion layer of the cathode can be alleviated by reacting with hydroniums migrated from the anolyte.[18,19] Nevertheless, the high proton concentration at the cathode surface often leads to HER dominance, significantly reducing the faradaic efficiency (FE) of eCO$_2$R.[20] To counteract this, alkali cations from the anolyte or cationic ionomers coated on the cathode surface are employed to create an electrostatic barrier, limiting excessive proton flux.[19,21–24] This, over time, would eventually cause salt precipitation and water flooding due to the rising local pH at the cathode surface as protons are consumed. Furthermore, reports on acidic MEAs with larger electrode areas (e.g., > 5 cm^2) remain scarce, highlighting a critical gap in scaling up this technology.

As an alternate solution to neutral/alkaline and acidic eCO$_2$R systems, bipolar membranes operated in forward bias (abbreviated here as f-BPM) have been explored to configure zero-gap MEAs, even enabling the use of pure water as the anolyte.[25] In a typical f-BPM setup, the AEM facing the cathode creates an alkaline environment conducive to selective CO_2 reduction, while the CEM facing the anode facilitates proton transport and blocks (bi)carbonate anion crossover.[26,27] Despite the improved CO_2 utilization, MEAs operated under the f-BPM mode face challenges of high cell voltage due to the large internal resistance, mechanical instability at the bipolar junction caused by mismatched CEM/AEM swelling rates, and stress accumulation from trapped CO_2 and H_2O.[28] To address these issues, researchers have contrived various tactics, including perforating the AEM to recirculate CO_2 and H_2O stalled in the junction,[29] direct membrane deposition via automated spray coating of AEM/CEM ionomers,[30] asymmetric BPM with differential AEM/CEM thickness,[31] and imprinting microfluidic channels into the bipolar junction.[32] While these efforts have advanced the field, most f-BPMs remain limited to short-term operation (tens of hours) and small form factors.

In this study, we address the persistent issues of blistering and delamination in f-BPMs[28–30] by designing a zero-gap MEA with an asymmetric porous bipolar junction. This architecture integrates electrospun fibrous AEMs with a planar CEM, leveraging the interconnected voids and channels within the nanofibers to alleviate mechanical stress caused by swelling mismatch and trapped water and gas. The biphasic nature of the electrospun nanofibers comprising hydrophobic polyvinylidene difluoride (PVDF) and ionic m-terphenyl p-terphenyl piperidinium copolymer (MTCP) enables the systemic tailoring of the ion transport, membrane swelling and mechanical strength. When operated under acidic conditions with alkaline cations, the resulting f-BPM not only suppresses cation migration—thereby inhibiting the HER and salt precipitation—but also facilitates CO_2 recirculation from the junction to the cathode, enhancing CO_2 utilization and reducing membrane stress (Scheme 1c). As a result, MEAs engaging the novel f-BPM
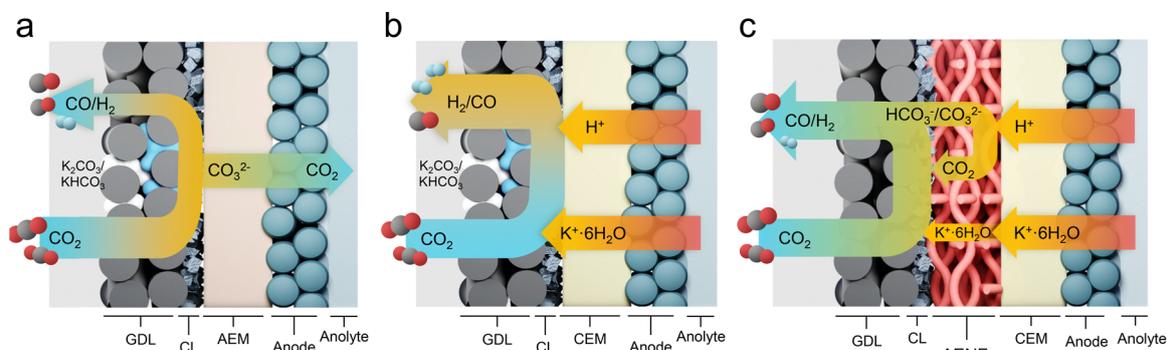
Scheme 1 Electrocatalytic CO_2 reduction (eCO$_2$R) in zero-gap membrane electrode assemblies (MEAs). (a) Alkaline/neutral conditions with AEM, (b) acidic conditions with CEM, and (c) acidic conditions with the bipolar AENFs/CEM proposed in this study.

architecture demonstrated a prolonged eCO$_2$R operation for 325 hours under acidic conditions with an average CO faradaic efficiency of 88%. A remarkable CO$_2$ utilization was attained at 300 mA cm^{-2} showcasing the single pass conversion (SPC) of 67% under 15 sccm of CO$_2$ flow. What's more, a 25 cm^2 f-BPM achieved stable operation over 110 hours with an energy efficiency of 34.2%, marking a significant step toward industrial feasibility.

Results

Fibrous membranes composed of the anion exchange ionomer (MTCP-50)[33] reinforced by PVDF were fabricated *via* the electrospinning method as detailed in the experimental section.

The chemical structure of MTCP-50, depicted in Fig. 1a, consists of a crosslinked copolymer with a 1:1 ratio of *m*-terphenyl and *p*-terphenyl piperidinium. This polymer has been reportedly manifesting high OH$^-$ ion conductivity (78.4 mS cm^{-1} at 30 °C) and ion exchange capacity (2.53 mmol g^{-1}), as well as a superb chemical stability in 1 M KOH for over 8000 hours.[33] By varying the MTCP/PVDF mass ratio (x), a series of anion-exchange nanofibers (denoted as AENF-x) were synthesized. The infrared (IR) spectrum taken on the exemplary AENF-1 confirmed the co-existence of both PVDF and MTCP-50 in the nanofibers (Fig. 1b). PVDF not only provides mechanical support, ensuring the durability of the nonwoven structure (Fig. 1c), but also modulates the hydrophobicity and swelling behavior of the composite, which are critical for regulating water and gas transport. Scanning electron microscopy (SEM)
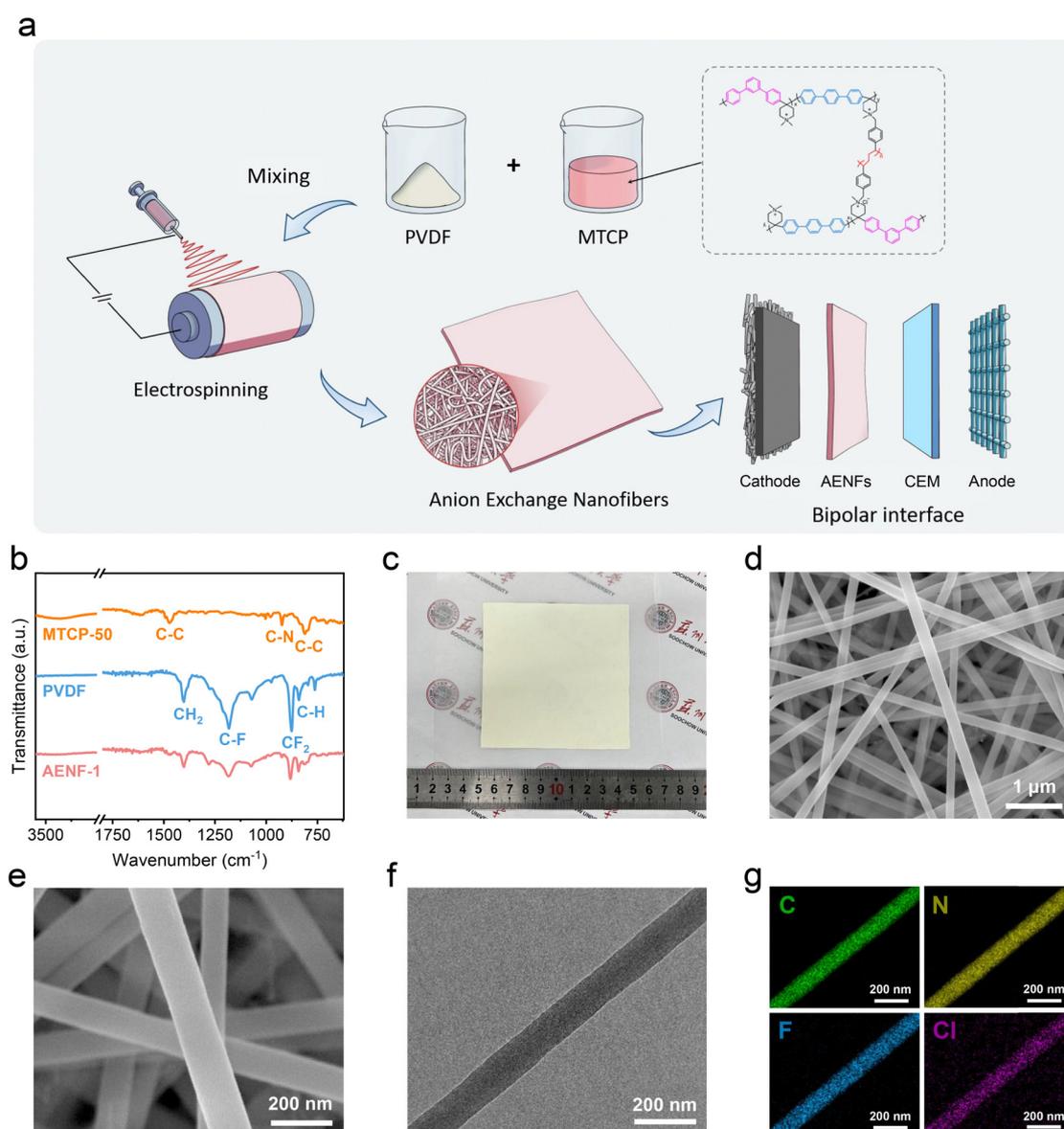

Fig. 1 Fabrication and characterization of AENFs. (a) Schematic illustration of the composition and fabrication of AENFs. (b) Infrared spectra of MTCP-50, PVDF and AENF-1. (c) Photograph, (d) and (e) SEM images of various magnifications, (f) TEM image, and (g) EDX elemental mapping images of AENF-1.

and transmission electron microscopy (TEM) images revealed that the nanofibers exhibit uniform thickness, with an average diameter of approximately 150 nm (Fig. 1d–f). Elemental mapping further confirmed the homogeneous distribution of carbon (C), nitrogen (N), fluorine (F), and chlorine (Cl) within the nanofibers (Fig. 1g). The interlaced fibers form tortuous voids and channels of varying sizes, which enhance mass transport properties that can be finely tuned by adjusting the MTCP/PVDF ratio (x) and thickness (y).

To investigate the impact of membrane thickness, AENF-1 (with a fixed MTCP/PVDF ratio, $x = 1$) was fabricated at three thicknesses: $y = 15 \pm 2$, 30 ± 2, and 60 ± 3 μm. Prior to use, all AENFs were sequentially treated with 1 M KOH and deionized (DI) water to activate the membrane. The gas permeability of AENF-1-y under wet conditions was evaluated using differential pressure tests.[29] Humidified CO_2 was forced through the wetted membrane in an MEA fixture, and the pressure drop across the membrane was monitored (Fig. S1). As expected, the gas permeability decreased with increasing membrane thickness, demonstrating a strong correlation between thickness and pressure drop (Fig. S2, ESI†). To assess mechanical strength, tensile tests were performed on wetted AENF-1-y membranes immediately after taking out from DI water (Fig. S3, ESI†). The results revealed a monotonic increase in mechanical strength with thickness, ranging from 4.48 MPa ($y = 15$ μm) to 16.67 MPa ($y = 60$ μm) (Fig. S4, ESI†).

Prior to electrochemical testing, we assembled a membrane electrode assembly (MEA) containing only a Nafion HP and AENF-1-y to assess their ability of suppressing H^+ migration (Fig. S5, ESI†).[34] AENF-1-60 maintained a higher pH (3.58) compared to the thinner AENF-1-15 (2.87) and CEM-only control sample (2.83) after 30 minutes. The enhanced suppression was attributed to the longer H^+ migration path and more cationic groups in the thicker membranes.

These findings highlight the critical role of membrane thickness in controlling H^+ crossover.

To further explore the effect of membrane thickness on eCO$_2$R performance, AENF-1-y was paired with Nafion-HP to form bipolar junctions in acidic MEAs. The cross-sectional images reveal the laminated structure of the carbon fiber paper (CFP), catalyst layer (CL) supported on the microporous layer (MPL), the AENF layer and the CEM, which confirm the intimate contact among GDE/CL/AENF-1/CEM (Fig. S6, ESI†). These MEAs were operated in forward-bias mode (f-BPM) using an anolyte of K_2SO_4/H_2SO_4 ($C_{K^+} = 0.05$ M, pH = 2) and an IrO$_x$-loaded titanium felt anode. The choice of K_2SO_4/H_2SO_4 with 0.05 M K^+ and pH = 2 was guided by the following considerations: (1) K^+ concentration optimization: systematic measurements of CO_2 reduction selectivity across varying K^+ concentrations (0.01–1 M) revealed that using electrolyte with 0.05 M K^+ achieves a balance between high faradaic efficiency (Fig. S7, ESI†) for target products ($> 95\%$) and long-term stability. Lower K^+ concentrations minimize salt precipitation and electrode flooding,[35] which are critical for sustained operation, while still providing sufficient K^+ to drive eCO$_2$R. (2) pH selection: pH = 2 was chosen based on prior computational and experimental

studies demonstrating its suitability for acidic eCO$_2$R.[14] Finite element simulations confirm that bulk-phase pH = 2 avoids CO_2 hydrolysis to bicarbonate/carbonate ions (CO_3^{2-}/HCO_3^-), thereby mitigating carbon loss via bicarbonate/carbonate formation and crossover. While localized pH near the catalyst surface rises during operation, the acidic bulk electrolyte (pH = 2) ensures rapid re-protonation of carbonate species to CO_2, maintaining adequate CO_2 availability at the reaction interface.

A highly porous Ni–N–C composite was synthesized for use as the cathode catalyst. The synthetic procedure is detailed in the ESI.† In brief, magnesium carbonate hydroxide served as a structural template, which was coated with a carbonaceous layer via chemical vapor deposition. Following template removal, nickel phthalocyanine (NiPc) molecules were loaded onto the carbon support and thermally annealed to form Ni–N–C complexes. SEM and TEM images revealed that the Ni–N–C composite adopts a nanosheet morphology composed of numerous hollow nanocubes (Fig. 2a and b). High-angle annular dark-field scanning transmission electron microscopy (HAADF-STEM) confirmed the homogeneous distribution of nitrogen (N) and nickel (Ni) elements across the carbon support (Fig. 2c). X-ray photoelectron spectroscopy (XPS) of the N 1s spectrum indicated that the nitrogen contents are highly heterogeneous, including oxidized, graphitic, pyrrolic, pyridinic, and coordinated Ni–N species. X-ray absorption near-edge structure (XANES) analysis revealed that the valence state of Ni lies between 0 and +2, consistent with single atomic Ni–N–C composites.[36,37] Fourier transform-extended X-ray absorption fine structure (FT-EXAFS) further supported this observation, showing no metallic Ni–Ni bonding but a prominent Ni–N peak at 1.4 Å. The high porosity of the carbon support, combined with the uniform dispersion of single-atom Ni sites, endows the Ni–N–C composite with exceptional catalytic activity for CO production in eCO$_2$R.[38,39]

In the eCO$_2$R tests of f-BPM engaging AENF-1 of varying thickness (Fig. S8, ESI†), the performance indices and process metrics taken into consideration include: (1) average cell voltage at 100 mA cm^{-2} during a 45-hour galvanostatic operation; (2) average faradaic efficiency of CO (FE$_{CO}$); (3) estimated crossover rate of K^+ from the anolyte; and (4) flooding rate of the cathode. The average flooding and K^+ crossover rates were estimated by collecting the cathodic effusion and quantifying the K^+ content via inductively coupled plasma-atomic emission spectrometry (ICP-OES). While the average cell voltage increased generally with membrane thickness, ranging from 3.45 V for AENF-1-15 to 3.68 V for AENF-1-60, AENF-1-30 exhibited the highest average FE$_{CO}$ of 95% (Fig. S9 and Table S1, ESI†). The flooding rate decreased with increasing thickness, while the K^+ crossover reached a minimum at $y = 30$ (Fig. S10, ESI†). However, further increasing the thickness to 60 μm led to a rebound in K^+ crossover, likely due to higher cell voltages exacerbating cation migration.[35] These results highlight the effectiveness of the bipolar junction in mitigating K^+ crossover and water flooding, attributed to the mixed cationic and hydrophobic properties of AENFs. Notably, lower cell voltages are desirable not only for energy efficiency but also
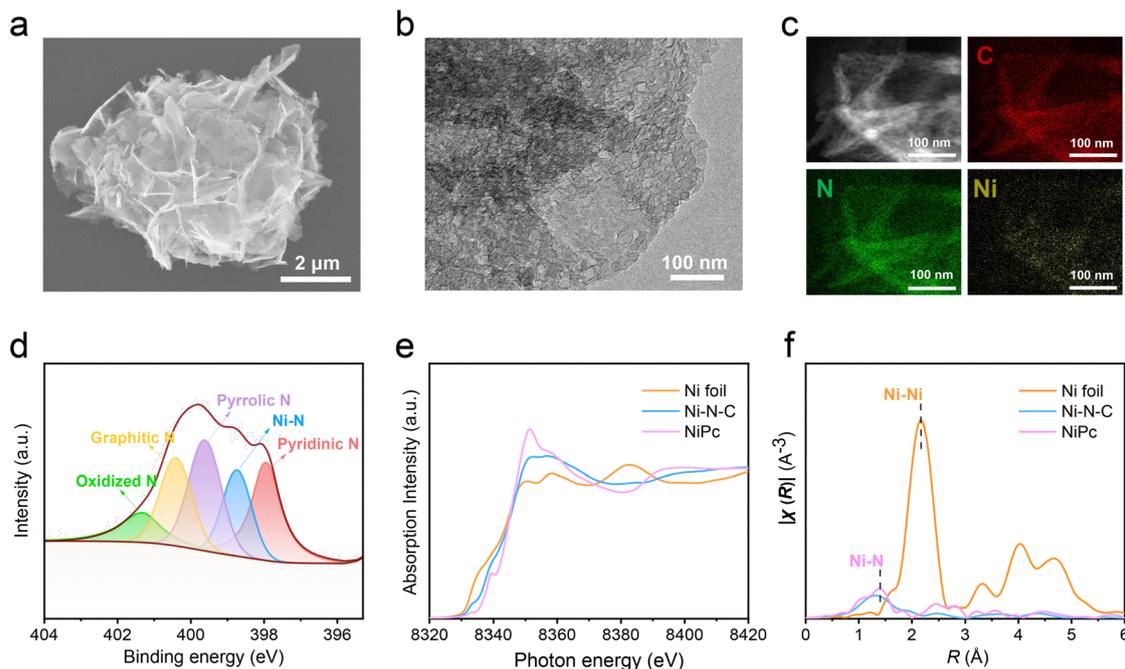
Fig. 2 Morphological and physico-chemical characterizations of the Ni–N–C catalyst. (a) SEM, (b) TEM, (c) HAADF–STEM elemental mapping images, and (d) XPS N 1s spectrum of the Ni–N–C catalyst. (e) XANES and (f) FT-EXAFS spectra of the Ni–N–C catalyst in reference to the Ni foil and nickel phthalocyanine.

for minimizing K^+ crossover. Based on these findings, AENF-1-30 (30 ± 2 μm) was identified as the optimal thickness, balancing performance and stability. Consequently, in subsequent studies, AENF-x refers to AENF-x-30. The lowest K^+ crossover rate was measured to be 1.37 mmol h^{-1} in the AENF system, which was higher than the values (0.015–0.135 mmol h^{-1}) reported in conventional AEM-based MEAs (Table S2, ESI†).[35,40,41] The high K^+ crossover in the AENF system can be attributed to its porous and loose nanofiber structure, which facilitates faster ion diffusion compared to dense AEMs.

After determining the optimal film thickness (y) using AENF-1, we continued to alter the MTCP/PVDF mass ratio (x) from 0.5 to 1, 2, and 3 to investigate its impact on membrane properties and eCO$_2$R metrics. SEM images showed that all AENF-x membranes were able to maintain an integral fibrous structure with similar fiber diameters (Fig. S11, ESI†). Infrared (IR) spectra further validated the coexistence of PVDF and MTCP-50 in the nanofibers, with characteristic peak intensities reflecting the changes in MTCP/PVDF ratio (Fig. S12, ESI†). Both water uptake and OH$^-$ conductivity measurements indicated that swelling and anion conductivity increased with higher MTCP content (Fig. 3a and b and Fig. S13, ESI†). This trend aligns with the well-established relationship between high ion-exchange capacity (IEC) and increased water uptake, which often leads to more pronounced swelling.[42–44] As a result, the gas permeability of AENF-x decreased with increasing MTCP/PVDF ratio, with the highest differential pressure observed at $x = 3$ (Fig. 3c). However, this improvement in ion conductivity came at the cost of mechanical strength. Tensile tests on wetted AENF-x membranes demonstrated a clear decline in mechanical robustness with

higher MTCP content, culminating in a tensile strength of just 3.26 MPa for AENF-3 (Fig. 3d). The poor mechanical strength of AENF-3, coupled with its reduced gas permeability, raises concerns about its long-term stability in f-BPM operations. Accumulated stress from regenerated water and gas within the junction could compromise performance over extended periods. The ability of suppressing H$^+$ migration for AENF-x was also evaluated (Fig. S14, ESI†). With increasing the MTCP ratio from 0.5 to 2, improved H$^+$ migration suppression ability was observed. But the AENF-3 sample exhibited inferior H$^+$ migration suppression compared to other variants, which should be attributed to its higher water uptake (31.25%), which enhanced H$^+$ migration.

When integrated with Nafion-HP to configure f-BPMs, all AENF-x samples demonstrated high CO selectivity (FE$_{CO}$ > 90%) at current densities below 300 mA cm^{-2} (Fig. 4a–d). This performance starkly contrasts with that of Nafion-HP alone as the CEM, which exhibited an initial FE$_{CO}$ of <75% at 100 mA cm^{-2}, followed by a continuous decline as the current density increased (Fig. 4e). Apparently, the anion-exchange nanofibers can effectively restrict H$^+$ migration and thereby mitigate the HER on the cathode. The performances of AENF-x were also much better than that of the control BPM case, in which MTCP-50 was cast into a planar film of 35 ± 3 μm (Table S3, ESI†) and pressed onto Nafion-HP (Fig. 4f). Such a 2D planar junction showed a high initial FE$_{CO}$ of 98% at 100 mA cm^{-2}, but quickly deteriorated to less than 40% at 500 mA cm^{-2}. In addition, the cell voltages of the control BPM across all current densities were significantly higher than those observed from other cases (Fig. 4g). Compared with AENF-1 as an
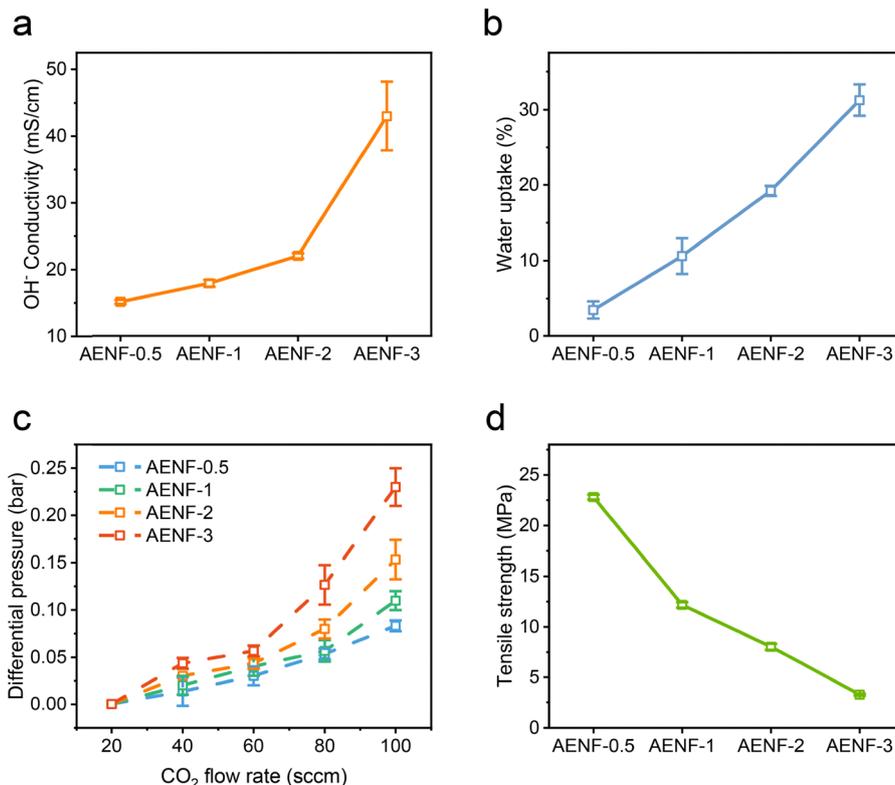
Fig. 3 Physico−chemical characterizations of AENF-x. (a) OH⁻ conductivity, (b) water uptake, (c) gas permeability and (d) mechanical strength under the wetted state.
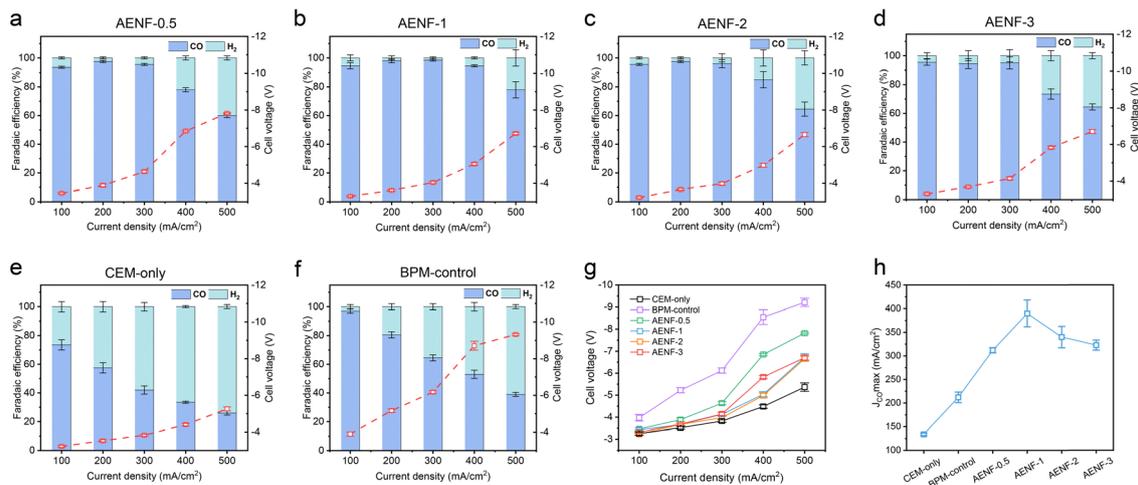

Fig. 4 Faradaic efficiencies of CO (left axis) and the corresponding cell voltages (right axis) at varying current densities recorded from MEAs of various f-BPM configurations: (a) AENF-0.5/Nafion-HP, (b) AENF-1/Nafion-HP, (c) AENF-2/Nafion-HP, (d) AENF-3/Nafion-HP, (e) Nafion-HP alone, and (f) 2D planar BPM composed of the casted MTCP-50 membrane and Nafion-HP. (g) Cell voltages at varying current densities recorded from MEAs of various f-BPM configurations. (h) J_{CO}max of various f-BPM configurations.

example, at 100 mA cm^{-2}, the voltage of AENF-1 (3.51 V) was 0.46 V lower than that of BPM-control (3.97 V).

Experimental investigation using a commercial anion-exchange ionomer (Sustainion® XA-9) to replace Nafion ionomer in the cathode catalyst layer with and without the AENF-1

layer was also conducted (Fig. S15, ESI†). The FE_{CO} is only $\sim$60% at 100 mA cm^{-2} and decreases to less than 35% with the current density increased to more than 200 mA cm^{-2} in the AENF-1/CEM configuration with Sustainion ionomer (Fig. S15a, ESI†). The FE_{CO} is only $\sim$80% at 100 mA cm^{-2} and decreases

to less than 50% with the current density increased to more than 200 mA cm^{-2} in the CEM-only configuration with the Sustainion ionomer (Fig. S15b, ESI†). Nafion ionomer exhibits superior FE$_{CO}$ than the anion-exchange Sustainion ionomer, which should be attributed to the Nafion ionomer serving as the cation-augmenting layer, which amplifies the cation effect to stabilize key *CO$_2^-$ intermediates and maintains high local pH in acidic eCO$_2$R. Such observation agrees well with a recent report which used a Nafion-K$^+$ interfacial cation matrix to boost selective eCO$_2$R in acid.[45] In contrast, anion-exchange ionomers like Sustainion®XA-9 lack this cation-concentrating capability, leading to suboptimal interfacial ion distribution and diminished eCO$_2$R selectivity.

Meanwhile, cell voltage breakdown analysis was systematically conducted using the reported method,[46] where the total cell voltage could be deconvoluted into thermodynamic potential, cathode overpotential (Fig. S16, ESI†), anode overpotential (Fig. S17, ESI†), ohmic loss (Fig. S18, ESI†), Nernstian pH loss, and other interfacial losses (see ESI† Note). The breakdown of cell voltages for different MEA configurations: CEM-only (3.23 V) and AENF-1 (3.51 V) are summarized in Fig. S19 and S20 (ESI†). The ohmic losses for the AENF/CEM and CEM-only configuration were 0.42 ± 0.01 V and 0.16 ± 0.02 V, respectively, which included the resistance of the membrane and electrode/membrane interface.[45] The voltage loss of the AENF-1 was estimated to be 0.26 V.

At higher current densities of 400 and 500 mA cm^{-2}, all AENF-x membranes exhibited increased H$_2$ production, accompanied by a significant rise in cell voltage. This strong correlation between H$_2$ yield and cell voltage underscores the detrimental impact of high cell voltages, which enhance both H$^+$ and K$^+$ migration. Increasing the MTCP/PVDF ratio from 0.5 to 1 reduced the full-cell voltage across all current densities, owing to the high ion conductivity of MTCP. However, further increasing the ratio to x = 2 and 3 did not yield substantial improvements in CO production, possibly due to the excessive membrane swelling and reduced gas permeability, which hinder CO$_2$ recirculation at the bipolar interface and restrict CO$_2$ supply at higher current densities. AENF-1 also demonstrated the highest CO partial current density of 390 mA cm^{-2}, which is three times that of the CEM-only case and 1.8 times that of the control BPM (Fig. 4h and 5a). This exceptional performance highlights the optimal balance between ion conductivity and swelling achieved by AENF-1, making it the preferred choice for the f-BPM configuration in this study. The results reveal a critical trade-off between ion conductivity and membrane swelling in modulating CO production. Additionally, the elevated cell voltage introduced by the bipolar junction partially offsets the benefits of Donnan exclusion in suppressing cation migration, adding more complexity to the system design.

To validate the reduction in K$^+$ and water permeation across the electrospun nanofibers with increasing MTCP content, K$^+$ crossover and water flooding rates were quantified using the previously described method (Fig. 5b). In the absence of a bipolar junction, Nafion-HP used as the standalone CEM

exhibited the highest levels of both K$^+$ crossover and water flooding. As the MTCP/PVDF ratio increased from 0.5 to 2, both K$^+$ crossover and water flooding were progressively suppressed. Compared to the CEM-only case, the lowest K$^+$ crossover and water flooding rates, achieved at x = 2, were reduced by 42% and 22%, respectively. However, for AENF-3 (x = 3), both the water flooding and K$^+$ crossover rates rebounded. This reversal is likely attributed to the poor mechanical stability of the highly swollen membrane and the dominance of the potential-driven electroosmotic effect over Donnan exclusion, leading to co-ion leakage.[17]

The operational stability of f-BPMs composed of AENF-x and Nafion-HP was evaluated in acidic MEAs under a galvanostatic current of 100 mA cm^{-2}. Among the four AENF-x samples with varying MTCP/PVDF ratios, AENF-1 demonstrated the highest stability, maintaining a CO faradaic efficiency (FE$_{CO}$) above 80% for over 300 hours (Fig. 5c and Fig. S21, ESI†). This result, with an average FE$_{CO}$ of 88% during the 325-h stability test, is among the best reported so far for acidic eCO$_2$R in MEA targeting CO generation (Fig. 5d and Table S4, ESI†). Additionally, the AENF-1-based MEA exhibited the lowest average cell voltage of 3.51 V, significantly outperforming AENF-0.5 (3.76 V, 40.5 h), AENF-2 (3.75 V, 52 h), and AENF-3 (3.82 V, 50 h). These results highlight the improved mass transport and minimized cell voltage achieved through the optimal BPM configuration, enhancing both energy efficiency and operational stability in acidic MEAs.

CO$_2$ utilization efficiency is a key advantage of MEAs operating under acidic conditions. Using the most stable AENF-1 configuration, we measured the single-pass conversion (SPC) of CO$_2$ at 300 mA cm^{-2} by varying the CO$_2$ flow rate from 15 to 60 sccm. As expected, the CO$_2$ conversion rate decreased with increasing flow rate, achieving a maximum SPC of 67% at 15 sccm and dropping to ∼18% at 60 sccm. Notably, the total CO$_2$ consumption remained nearly constant across all flow rates, as quantified by multiplying the flow rate by the conversion rate. This indicates that the CO$_2$ conversion is primarily limited by the MEA's treatment capacity, which is approximately 10 sccm at 300 mA cm^{-2}. Under these conditions, the highest CO yield reached 9.6 mL min^{-1} (sccm), equivalent to 25.7 mmol h^{-1}.

The electrospinning method employed to fabricate AENF-x membranes is readily scalable, enabling the production of large-area membranes (Fig. S22, ESI†). This scalability facilitates the adoption of BPMs with larger form factors. For demonstration, we constructed a 25-cm^2 MEA by paring AENF-1 with Nafion-HP, as shown in Fig. 6a. The scaled-up MEA achieved near-unity CO faradaic efficiency (FE$_{CO}$) at current densities of 100 and 200 mA cm^{-2} (Fig. 6b). Even at 300 mA cm^{-2}, with a total operating current of 7.5 A, the FE$_{CO}$ remained above 90%. More remarkably, the MEA was able to maintain a stable operation for over 110 hours before the FE$_{CO}$ dropped below 80%, with an average cell voltage of 3.41 V and an average FE$_{CO}$ of 87.1% (Fig. 6c). This performance corresponds to an impressive energy efficiency of 34.2% averaged over the entire testing period, underscoring the potential for industrial-scale deployment.
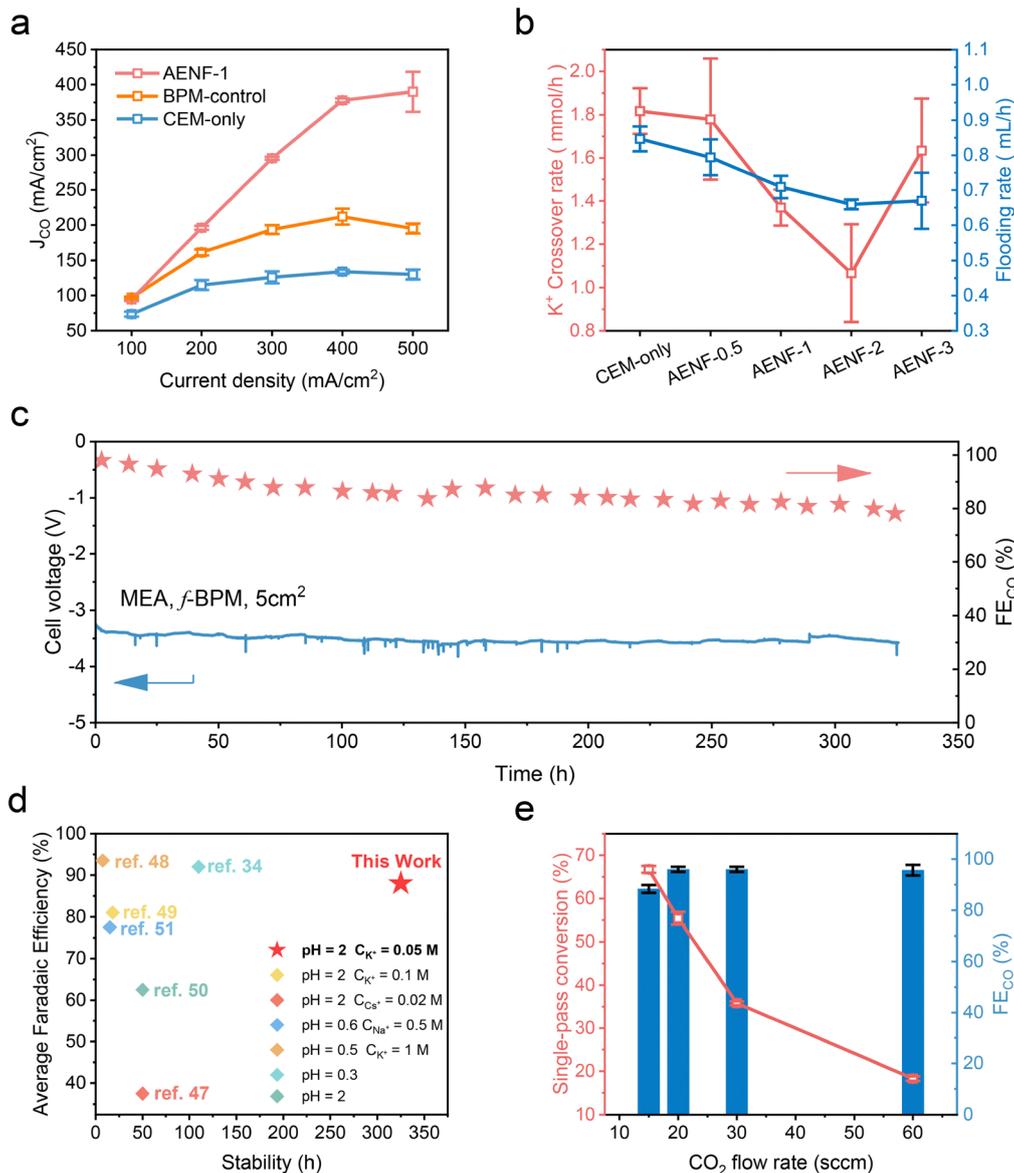
Fig. 5 eCO$_2$R performance of AENF-1 in a 5 cm^2 acidic MEA setup. (a) Comparison of partial CO current densities for the cases of AENF-1/Nafion-HP, BPM-Control and CEM-only. (b) Measured K$^+$ crossover and flooding rates for AENF-x in reference to the CEM-only case. (c) Long-term stability test at 100 mA cm^{-2} with AENF-1. (d) Comparison of the eCO$_2$R performance in this work with state-of-the-art literature results.[34,47–51] (e) Single-pass conversion of CO$_2$ at 300 mA cm^{-2} under different CO$_2$ flow rates.

Discussion

Our MEA operations, utilizing asymmetric porous bipolar junctions of AENF-x/Nafion-HP and an acidic anolyte of K$_2$SO$_4$/H$_2$SO$_4$ (C_{K^+} = 0.05 M, pH = 2), uncovered a highly complex interplay of structural and process parameters in eCO$_2$R. Key factors such as film thickness, nanofiber composition, membrane swelling, mechanical strength, and full-cell voltage collectively influence product selectivity and operational stability.

1. Both K$^+$ and H$^+$ migration correlate with the cell voltage, which is significantly affected by the properties of AENFs at the bipolar junction. A critical trade-off exists between the application of AENFs to suppress cation migration (*via* Donnan

exclusion) and the increased cell voltage it introduced to counteract this effect. Therefore, increasing the AENF film thickness inhibits K$^+$ crossover and HER but would be offset by the escalated cell voltage. Similarly, higher MTCP ratios in the nanofibers reduce K$^+$ and H$^+$ crossover but exacerbate swelling, leading to augmented electroosmosis, hindered CO$_2$ recirculation, and compromised mechanical stability.

2. Achieving a delicate balance among ion conductivity, membrane swelling, and mechanical strength is essential for the AENF at the bipolar junction. This balance can be finely tuned by adjusting the MTCP/PVDF ratio in the electrospun nanofibers. An optimal nanofiber structure, characterized by efficient anion transport, effective cation suppression, and
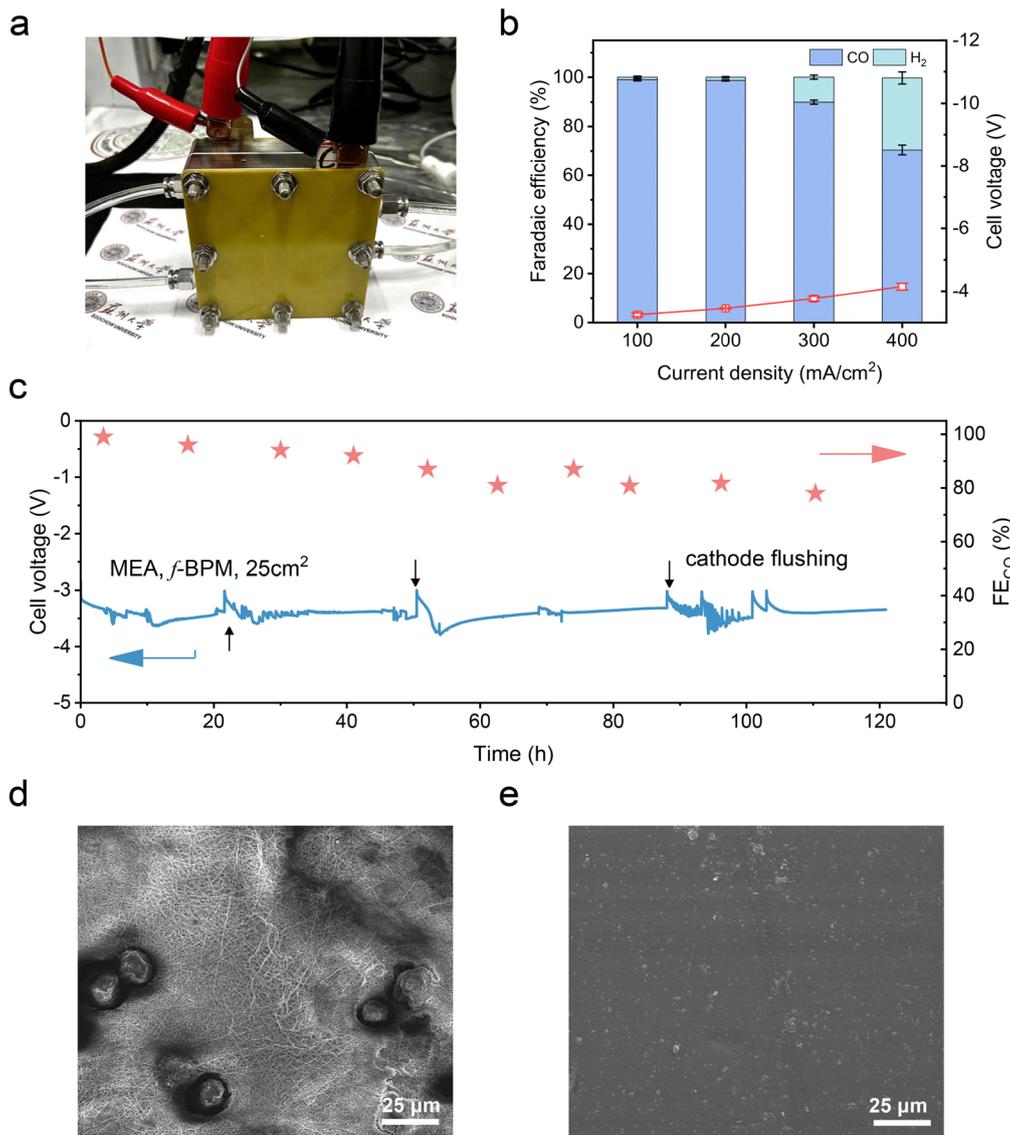
Fig. 6 eCO$_2$R performance of a 25-cm^2 MEA setup employing AENF-1/Nafion-HP as the f-BPM under acidic conditions. (a) Photograph of the MEA with a BPM form factor of 5 cm × 5 cm. (b) Faradaic efficiencies (left axis) and the corresponding cell voltages (right axis) at varying current densities. (c) Long term stability test at 100 mA cm^{-2}. (d) and (e) Top-view SEM images of the disassembled post-electrolytic AENF-1 and Nafion-HP membranes, respectively, for failure analysis.

moderate swelling, facilitates the recirculation of CO$_2$ and H$_2$O generated at the bipolar junction, thereby enhancing both operational stability and CO$_2$ utilization.

3. K$^+$ crossover and water flooding are mutually reinforcing challenges in MEA operation. Severe salt precipitation from K$^+$ crossover can clog gas channels in the gas diffusion electrode (GDE), impeding CO$_2$ mass transport and exacerbating the HER. This eventually compromises the GDE's hydrophobicity, leading to severe water flooding. On the other hand, the electroosmotic effect associated with K$^+$ migration draws excess water from the anolyte through the ion exchange membrane, further aggravating water flooding. To address these issues, maintaining a triphasic balance at the GDE interface is crucial. The current study achieves this balance

through a bipolar junction design featuring interlaced anion-exchange nanofibers.

4. The failure mechanism of the MEAs after prolonged operation was scrutinized by carefully inspecting the disassembled device components, including the IrO$_x$/Ti anode, Ni–N–C cathode and AENF-1/Nafion-HP BPM. Both morphological and chemical state analyses revealed negligible changes in the cathode and anode catalysts following hundreds of hours of electrolysis (Fig. S23–S26, ESI†). Additionally, elemental analyses on the cathode effusion and anolyte *via* ICP-OES detected no leaching of Ni and Ir (Table S5, ESI†), indicating that the performance decay was unlikely caused by catalyst degradation. IR spectra of AENF-1 and Nafion-HP before and after prolonged operation showed no significant changes in

chemical properties (Fig. S27 and S28, ESI†). However, SEM images of the disassembled f-BPM revealed sporadic blemished spots on the AENFs side, characterized by physically damaged and agglomerated fibers (Fig. 6d and Fig. S29, ESI†). In contrast, Nafion-HP remained intact. The blemished spots could be attributed to physical swelling and destruction of the fibrous structure caused by severe mechanical stress, inhomogeneous resistivity, and localized heating, collectively impairing the mass transport and ion-gating properties of the AENFs and ultimately leading to performance decay. Therefore, in future studies, it is necessary to further improve the durability of the AENFs to sustain harsher operational conditions at industrial scale.

Conclusion

In this work, we developed an asymmetric porous f-BPM architecture through the integration of electrospun AEM with two-dimensional planar CEM to address the critical challenges of CO_2 selectivity, salt precipitation, and water flooding in acidic MEA operations. The biphasic AENFs, composed of polycationic MTCP-50 and hydrophobic PVDF, were engineered to simultaneously optimize ion conductivity, membrane swelling resistance, and mechanical robustness, enabling synergistic modulation of cation migration, electrokinetic impedance, and water/gas transport properties. Through systematic optimization, AENF-1-30, featuring an optimal MTCP/PVDF ratio and moderate membrane thickness, demonstrated superior eCO_2R performance by effectively suppressing cation migration, alleviating BPM interfacial stress, and enhancing CO_2 utilization efficiency.

The acidic MEA system incorporating the optimized f-BPM configuration achieved remarkable stability, maintaining continuous operation for over 325 hours at 100 mA cm^{-2} with an average FE_{CO} of 88%, representing one of the highest reported values in the literature. Notably, the system exhibited exceptional CO_2 utilization efficiency, achieving a high SPC of 67% at 300 mA cm^{-2} with a CO_2 feed rate of 15 sccm. To demonstrate practical scalability, we successfully fabricated a larger 5 cm × 5 cm BPM, which maintained stable operation for 110 hours with a remarkable energy efficiency of 34.2% – the best reported so far for acidic MEA systems at this scale. These findings establish a new benchmark for acidic CO_2 electrolysis and pave the way for future investigations focusing on advanced anion-exchange chemistries and polymer matrices to enable thousand-hour stable operation under industrially relevant conditions.

Data availability

Further information and requests for resources should be directed to and will be fulfilled by the corresponding author.

Conflicts of interest

The authors declare no conflict of interest.

References

1 S. Jordaan and C. Wang, *Nat. Catal.*, 2021, **4**, 915–920.
2 G. Wang, J. Chen, Y. Ding, P. Cai, L. Yi, Y. Li, C. Tu, Y. Hou, Z. Wen and L. Dai, *Chem. Soc. Rev.*, 2021, **50**, 4993–5061.
3 C. O'Brien, R. Miao, A. Zeraati, G. Lee, E. Sargent and D. Sinton, *Chem. Rev.*, 2024, **124**, 3648–3693.
4 S. Nitopi, E. Bertheussen, S. Scott, X. Liu, A. Engstfeld, S. Horch, B. Seger, I. Stephens, K. Chan, C. Hahn, J. Norskov, T. Jaramillo and I. Chorkendorff, *Chem. Rev.*, 2019, **119**, 7610–7672.
5 H. Shin, K. Hansen and F. Jiao, *Nat. Sustainable.*, 2021, **4**, 911–919.
6 R. I. Masel, Z. Liu, H. Yang, J. J. Kaczur, D. Carrillo, S. Ren, D. Salvatore and C. P. Berlinguette, *Nat. Nanotechnol.*, 2021, **16**, 118–128.
7 T. Burdyny and W. Smith, *Energy Environ. Sci.*, 2019, **12**, 1442–1453.
8 L. Ge, H. Rabiee, M. Li, S. Subramanian, Y. Zheng, J. Lee, T. Burdyny and H. Wang, *Chem*, 2022, **8**, 663–692.
9 Z. Zhang, X. Huang, Z. Chen, J. J. Zhu, B. Endrödi, C. Jánáky and D. H. Deng, *Angew. Chem., Int. Ed.*, 2023, **62**, e202302789.
10 J. A. Rabinowitz and M. W. Kanan, *Nat. Commun.*, 2020, **11**, 5231.
11 T. H. Ha, J. Kim, H. Choi and J. Oh, *ACS Energy Lett.*, 2024, **9**, 4835–4842.
12 X.-F. Qiu, H.-L. Zhu, J.-R. Huang, P.-Q. Liao and X.-M. Chen, *J. Am. Chem. Soc.*, 2021, **143**, 7242–7246.
13 J. E. Huang, F. W. Li, A. Ozden, A. S. Rasouli, F. P. G. de Arquer, S. J. Liu, S. Z. Zhang, M. C. Luo, X. Wang, Y. W. Lum, Y. Xu, K. Bertens, R. K. Miao, C. T. Dinh, D. Sinton and E. H. Sargent, *Science*, 2021, **372**, 1074–1078.
14 Y. Xie, P. Ou, X. Wang, Z. Xu, Y. Li, Z. Wang, J. Huang, J. Wicks, C. McCallum, N. Wang, Y. Wang, T. Chen, B. Lo, D. Sinton, J. Yu, Y. Wang and E. Sargent, *Nat. Catal.*, 2022, **5**, 564–570.
15 Y. Zhao, L. Hao, A. Ozden, S. Liu, R. K. Miao, P. Ou, T. Alkayyali, S. Zhang, J. Ning, Y. Liang, Y. Xu, M. Fan, Y. Chen, J. E. Huang, K. Xie, J. Zhang, C. P. O'Brien, F. Li, E. H. Sargent and D. Sinton, *Nat. Synth.*, 2023, **2**, 403–412.

16 M. Zeng, W. Fang, Y. Cen, X. Zhang, Y. Hu and B. Xia, *Angew. Chem., Int. Ed.*, 2024, **63**, e202404574.

17 J. C. Bui, E. W. Lees, D. H. Marin, T. N. Stovall, L. Chen, A. Kusoglu, A. C. Nielander, T. F. Jaramillo, S. W. Boettcher, A. T. Bell and A. Z. Weber, *Nat. Chem. Eng.*, 2024, **1**, 45–60.

18 M. Rashid, S. Nabil, M. Adnan, K. Kannimuthu and M. Kibria, *Adv. Energy Mater.*, 2024, **14**, 202400570.

19 Q. Bai, L. Xiong, Y. Zhang, M. Ma, Z. Jiao, F. Lyu, Z. Deng and Y. Peng, *EES Catal.*, 2024, **2**, 1228–1237.

20 T. Ha, J. Kim, H. Choi and J. Oh, *ACS Energy Lett.*, 2024, **9**, 4835–4842.

21 J. Gu, S. Liu, W. Ni, W. Ren, S. Haussener and X. Hu, *Nat. Catal.*, 2022, **5**, 268–276.

22 Z. Ma, Z. Yang, W. Lai, Q. Wang, Y. Qiao, H. Tao, C. Lian, M. Liu, C. Ma, A. Pan and H. Huang, *Nat. Commun.*, 2022, **13**, 7596.

23 B. Pan, Y. Wang and Y. Li, *Chem. Catal.*, 2022, **2**, 1267–1276.

24 M. Fan, J. Huang, R. Miao, Y. Mao, P. Ou, F. Li, X. Li, Y. Cao, Z. Zhang, J. Zhang, Y. Yan, A. Ozden, W. Ni, Y. Wang, Y. Zhao, Z. Chen, B. Khatir, C. O'Brien, Y. Xu, Y. Xiao, G. Waterhouse, K. Golovin, Z. Wang, E. Sargent and D. Sinton, *Nat. Catal.*, 2023, **6**, 763–772.

25 X. She, L. Zhai, Y. Wang, P. Xiong, M. Li, T. Wu, M. Wong, X. Guo, Z. Xu, H. Li, H. Xu, Y. Zhu, S. Tsang and S. Lau, *Nat. Energy*, 2024, **9**, 154–162.

26 Y. Li, Z. Yan, J. Hitt, R. Wycisk, P. Pintauro and T. Mallouk, *Adv. Sustainable Syst.*, 2018, **2**, 1700187.

27 D. Song, Y. Lian, M. Wang, Y. Su, F. Lyu, Z. Deng and Y. Peng, *eScience*, 2023, **3**, 100097.

28 R. Fischer, M. Dessiex, F. Marone and F. Büchi, *ACS Appl. Energy Mater.*, 2024, **7**, 3590–3601.

29 J. Disch, S. Ingenhoven and S. Vierrath, *Adv. Energy Mater.*, 2023, **13**, 202400570.

30 T. Alkayyali, A. S. Zeraati, H. Mar, F. Arabyarmohammadi, S. Saber, R. K. Miao, C. P. O'Brien, H. Liu, Z. Xie, G. Wang, E. H. Sargent, N. Zhao and D. Sinton, *ACS Energy Lett.*, 2023, **8**, 4674–4683.

31 M. Hesselmann, J. Lee, S. Chae, A. Tricker, R. Keller, M. Wessling, J. Su, D. Kushner, A. Weber and X. Peng, *ACS Appl. Mater. Interfaces*, 2024, **16**, 24649–24659.

32 Y. Xu, R. Miao, J. Edwards, S. Liu, C. O'Brien, C. Gabardo, M. Fan, J. Huang, A. Robb, E. Sargent and D. Sinton, *Joule*, 2022, **6**, 1333–1343.

33 W. Song, K. Peng, W. Xu, X. Liu, H. Zhang, X. Liang, B. Ye, H. Zhang, Z. Yang, L. Wu, X. Ge and T. Xu, *Nat. Commun.*, 2023, **14**, 2732.

34 B. Wu, B. Wang, B. Cai, C. Wu, W. W. Tjiu, M. Zhang, Z. Aabdin, S. Xi and Y. Lum, *J. Am. Chem. Soc.*, 2024, **146**, 29801–29809.

35 S. Hao, A. Elgazzar, N. Ravi, T.-U. Wi, P. Zhu, Y. Feng, Y. Xia, F.-Y. Chen, X. Shan and H. Wang, *Nat. Energy*, 2025, **10**, 266–277.

36 W. Hua, H. Sun, H. Lin, Q. Mu, B. Yang, Y. Su, H. Wu, F. Lyu, J. Zhong, Z. Deng and Y. Peng, *Chem. Eng. J.*, 2022, **446**, 137296.

37 H. Wang, X. Wu, G. Liu, S. Wu and R. Xu, *Nano Res.*, 2023, **16**, 4546–4553.

38 P. Su, K. Iwase, S. Nakanishi, K. Hashimoto and K. Kamiya, *Small*, 2016, **12**, 6083–6089.

39 C. Lv, K. Huang, H. Xu, G. Sun, H. Zheng, C. Lian, Y. Zhang, C. Ma, J. Wang and L. Ling, *ACS Sustainable Chem. Eng.*, 2024, **12**, 11901–11912.

40 S. Kato, S. Ito, S. Nakahata, R. Kurihara, T. Harada, S. Nakanishi and K. Kamiya, *ChemSusChem*, 2024, **17**, e202401013.

41 J. Biemolt, J. Singh, G. Prats Vergel, H. M. Pelzer and T. Burdyny, *ACS Energy Lett.*, 2025, **10**, 807–814.

42 N. Chen and Y. Lee, *Trends Chem.*, 2022, **4**, 236–249.

43 S. Garg, C. Rodriguez, T. Rufford, J. Varcoe and B. Seger, *Energy Environ. Sci.*, 2022, **15**, 4440–4469.

44 S. Favero, I. Stephens and M. Titirci, *Adv. Mater.*, 2024, **36**, 2308238.

45 A. Shayesteh Zeraati, F. Li, T. Alkayyali, R. Dorakhan, E. Shirzadi, F. Arabyarmohammadi, C. P. O'Brien, C. M. Gabardo, J. Kong, A. Ozden, M. Zargartalebi, Y. Zhao, L. Fan, P. Papangelakis, D. Kim, S. Park, R. K. Miao, J. P. Edwards, D. Young, A. H. Ip, E. H. Sargent and D. Sinton, *Nat. Synth.*, 2025, **4**, 75–83.

46 K. Xie, R. K. Miao, A. Ozden, S. J. Liu, Z. Chen, C. T. Dinh, J. E. Huang, Q. C. Xu, C. M. Gabardo, G. Lee, J. P. Edwards, C. P. O'Brien, S. W. Boettcher, D. Sinton and E. H. Sargent, *Nat. Commun.*, 2022, **13**, 3609.

47 B. Pan, J. Fan, J. Zhang, Y. Luo, C. Shen, C. Wang, Y. Wang and Y. Li, *ACS Energy Lett.*, 2022, **7**, 4224–4231.

48 H. Li, H. Li, P. Wei, Y. Wang, Y. Zang, D. Gao, G. Wang and X. Bao, *Energy Environ. Sci.*, 2023, **16**, 1502–1510.

49 M. Wang, L. Lin, Z. Y. Zheng, Z. Y. Jiao, W. Hua, G. W. Wang, X. X. Ke, Y. B. Lian, F. Lyu, J. Zhong, Z. Deng and Y. Peng, *Energy Environ. Sci.*, 2023, **16**, 4423–4431.

50 J. Fan, B. Pan, J. Wu, C. Shao, Z. Wen, Y. Yan, Y. Wang and Y. Li, *Angew. Chem., Int. Ed.*, 2024, **63**, e202317828.

51 Z. Liu, T. Yan, H. Shi, H. Pan, Y. Cheng and P. Kang, *ACS Appl. Mater. Interfaces*, 2022, **14**, 7900–7908.